NASA Technical Memorandum 83575

Comparison of Secondary Flows Predicted by a Viscous Code and an Inviscid Code With Experimental Data for a Turning Duct

John R. Schwab and Louis A. Povinelli
Lewis Research Center
Cleveland, Ohio

Prepared for the
Symposium on Computation of Internal Flows:
Methods and Applications
sponsored by the American Society of Mechanical Engineers
New Orleans, Louisiana, February 13-15, 1984

NASA

COMPARISON OF SECONDARY FLOWS PREDICTED BY A VISCOUS CODE AND AN INVISCID CODE WITH EXPERIMENTAL DATA FOR A TURNING DUCT

John R. Schwab and Louis A. Povinelli
National Aeronautics and Space Administration
Lewis Research Center
Cleveland, Ohio 44135

SUMMARY

A comparison of the secondary flows computed by the viscous Kreskovsky-Briley-McDonald code and the inviscid Denton code with benchmark experimental data for a turning duct is presented. The viscous code is a fully parabolized space-marching Navier-Stokes solver while the inviscid code is a time-marching Euler solver. The experimental data were collected by Taylor, Whitelaw, and Yianneskis with a laser doppler velocimeter system in a 90° turning duct of square cross-section. The agreement between the viscous and inviscid computations was generally very good for the streamwise primary velocity and the radial secondary velocity, except at the walls, where slip conditions were specified for the inviscid code. The agreement between both the computations and the experimental data was not as close, especially at the 60.0° and 77.5° angular positions within the duct. This disagreement was attributed to incomplete modelling of the vortex development near the suction surface.

INTRODUCTION

The continued emphasis on secondary flow problems in the design and analysis of turbomachinery requires three-dimensional flow prediction capable of accurately modelling secondary flows. Three-dimensional elliptic Navier-Stokes codes such as those developed by Hah (ref. 1) have been shown to predict cascade secondary flows fairly well. However, such codes require large amounts of computer storage and long computation times, thus precluding their use for routine design and analysis of turbomachinery geometries at the present time. This situation is expected to change with further developments in computer architecture and algorithm optimization. Meanwhile, three-dimensional parabolized Navier-Stokes codes such as the Kreskovsky-Briley-McDonald code (ref. 2) and three-dimensional Euler codes such as the Denton code (ref. 3) can provide valuable information about secondary flows while requiring less computer storage and shorter computation times than an elliptic Navier-Stokes solver.

This paper compares the secondary flows predicted by the inviscid Denton code and the viscous Kreskovsky-Briley-McDonald code with experimental data for a 90° turning duct of square cross-section taken by Taylor, Whitelaw, and Yianneskis (ref. 4). The experiment was performed in order to provide benchmark data for use in computer code assessment. While the turning duct is a rather simple geometry compared to a turbomachine blade row, it allows much less cumbersome experimental technique to be used and fairly simple grid generation. In addition, the secondary flows generated in a turning duct are less complex than those found in a blade row. The results presented in this paper consist of streamwise primary and radial secondary velocity profiles and secondary flow vector plots at various angular positions in the duct.

SYMBOLS

De	Dean number, $De = (d/2r_c)^{1/2}\ Re$
d	hydraulic diameter
h	duct spanwise height
Re	Reynolds number, $Re = d\bar{V}/\nu$
r	radial coordiate
r*	normalized radial coordinate, $r^* = (r - r_o)/(r_i - r_o)$
r_c	mean radius of curvature, $r_c = (r_i + r_o)/2$
r_i	inner radius of curvature (suction surface)
r_o	outer radius of curvature (pressure surface)
$\bar{V}$	bulk mean velocity
V_θ	streamwise velocity component
V_r	radial velocity component
V_z	spanwise velocity component
w	duct radial width
z	spanwise coordinate
z*	mormalized spanwise coordinate, $z^* = z/h$
θ	streamwise coordinate
ν	kinematic viscosity

METHOD

Inviscid Computation

The inviscid code, described in reference 3, is an explicit time-marching solution of the unsteady Euler equations in finite-volume form. A two-level multigrid technique is used to reduce computation time while variable time steps and linear smoothing are employed to control instability. The uniformly spaced grid used for the turning duct computations consisted of 21 points in the radial direction between the pressure and suction surfaces, 21 points in the spanwise direction between the endwalls, and 75 points in the streamwise direction. The grid is shown in figure 1.

The inviscid code originally had provisions for inlet total pressure shear in only the spanwise direction; modifications were made to allow a full specification of the inlet total pressure field with shear in both transverse directions. This field was calculated from data presented in reference 4. Slip conditions at the walls were specified as the total pressure corresponding to 30 percent of the maximum freestream velocity for the inlet plane. Preliminary computations with lower velocity slip conditions were subject to instability and would require large amounts of smoothing to obtain a converged solution with consequent numerical viscosity effects. The smoothing used in this computation was limited to the minimum required to prevent decoupling of the solution on adjacent grid points.

The uniform transverse grid spacing was considered to be adequate, since 4 grid points were located within the boundary layer and more exacting resolution at the walls would be meaningless, given the slip approximation required for an inviscid computation. Since the inviscid code could not be run at incompressible velocities for this case, the average velocity over the entire flow field was set at a Mach number of 0.3 to allow some density variation in the conservation variables while minimizing gross compressibility effects because the viscous computation was incompressible and the experimental data was for a water tunnel. Typical CPU execution times for these computations using the 21 x 21 x 75 grid were 60 to 75 min on an IBM 3033 and 10 to 15 min on a CRAY-1.

Viscous Computation

The results from the viscous computation were taken from reference 2. The viscous code is based upon a primary-secondary velocity decomposition method which produces a set of approximate governing equations to correct an inviscid potential flow solution for viscous effects, secondary flows, and pressure field distortion. Finite-difference formulations of the correction equations are solved as an initial-value problem in space by an implicit single-pass forward-marching technique. The method assumes that streamwise diffusion is negligible and that the bulk pressure correction included in the streamwise momentum equations is uniform over each cross section; thus, it may be categorized as a "fully parabolized Navier-Stokes" solver (ref. 5). The grid used consisted of 30 radial points, 20 spanwise points between the endwall and the plane of symmetry and 25 streamwise points between $\theta = 0°$ and $\theta = 77.5°$. The transverse grid was locally refined near the walls. Typical CPU execution times for this computation were approximately 4 min on a CDC 7600, which would correspond roughly to 7 to 8 min on an IBM 3033 or 1 to 2 min on a CRAY-1. These times do not include the execution time for the a priori potential solution.

Experimental Data

The experimental data were taken from reference 4, where laser doppler velocimetry was used to measure primary and secondary flows in water through a 90° turning duct of 40 mm x 40 mm square cross-section with a curvature ratio, r_c/w, of 2.3. As a consequence of the uniform cross-sectional area, both curvature and pressure gradient effects were present in the duct. The inlet boundary layers on the pressure and suction surfaces and on the endwalls were found to be 15 percent of the hydraulic diameter at a Reynolds number of 40 000 and a Dean number of 18 700. Measurements were obtained at the inlet and exit survey planes shown in figure 2 and at angular positions of 30.0°, 60.0°, and 77.5° in spanwise increments of 5 percent and radial increments of 20 percent beginning at 10 percent away from the pressure surface.

RESULTS AND DISCUSSION

Qualitative Flow Features

The secondary flow field computed by the inviscid code is shown in figures 3 to 5 for the 30.0°, 60.0°, and 77.5° positions respectively.

These secondary flow vectors are computed as vector deviations from the grid lines, but should approximate the true secondary flows as long as the grid lines approximate the true streamlines. The development of two symmetrical vortices about the midspan position is clearly discernable at the 30.0° position. The secondary flow moves along the sidewalls of the duct from the pressure side to the suction side in the positive radial coordinate direction. The magnitude of the secondary flow increases significantly as the flow moves downstream to the 60.0° and 77.5° positions. At the 60.0° position, shown in figure 4, the vortex cores have been intensified and at the 77.5° position, shown in figure 5, the magnitude of the velocities and the extent of the vortex cores have been strongly developed. The secondary flow field at the duct outlet 100 mm downstream of the bend is shown in figure 6, where the magnitude of the secondary velocities has diminished and the two vortices have become slightly asymmetrical. The asymmetry may be caused by grid skew that is inherent in the grid generation algorithm used with the inviscid code.

In order to make quantitative comparisons of the inviscid and viscous computational results with the experimental data, plots of both streamwise primary and radial secondary velocities were made at fixed distances from the pressure surface to the suction surface ($r^* = 0.1$ to $r^* = 0.9$) as a function of distance from the endwall to the midspan position ($z^* = 0.0$ to $z^* = 0.5$). These are discussed in the following sections.

Primary Velocity Profiles

The streamwise primary velocity profiles from the inviscid and viscous computations and the experimental data are shown in figures 7 to 9 for angular positions of 30.0°, 60.0°, and 77.5° within the duct. Plots are shown in each figure for constant values of r^*, beginning near the pressure surface at $r^* = 0.1$ and ending near the suction surface at $r^* = 0.9$. The velocities are normalized by the bulk mean velocity, $\bar{V}$. In general, the agreement between the inviscid and viscous computations is very good, except near the walls where slip conditions were required for the inviscid code. The computations match the experimental data closely near the pressure surface for $r^* = 0.1$ to $r^* = 0.5$; however, near the suction surface for $r^* = 0.7$ to $r^* = 0.9$, the agreement is not as close, especially at the 60.0° and 77.5° positions. This can be attributed to large distortion of the primary flow by strong vortex flow that is modelled incompletely by both the inviscid and viscous computations. The same trends are indicated in figure 10, where the experimental data and the inviscid computation for the duct outlet position are presented. Results from the viscous computation were not available since it was terminated at the 77.5° position in reference 2.

Secondary Velocity Profiles

The radial secondary velocity profiles from the inviscid and viscous computations and the experimental data are shown in figures 11 to 13 for angular positions of 30.0°, 60.0°, and 77.5° within the duct. The velocities are normalized by the bulk mean velocity, $\bar{V}$. Both computations match the experimental data near the pressure surface, but the agreement becomes progressively worse near the suction surface. The inviscid computation overpredicts the radial velocities at the endwalls ($z^* = 0.0$) due to the slip boundary con-

ditions. This effect is very pronounced from $r^* = 0.5$ to $r^* = 0.9$ for the 60.0° position (fig. 12) and from $r^* = 0.7$ to $r^* = 0.9$ for the 77.5° position (fig. 13). The strong reversals in the experimental data at $r^* = 0.9$ and $z^* = 0.35$ for the 60.0° and 77.5° positions clearly indicate vortex formation that both the inviscid and the viscous computations do not show.

The disagreement between the inviscid computation and the experimental data near the suction surface extends over most of the duct height as the vortex flow becomes more strongly developed at the 77.5° position. This behavior indicates that the inviscid computation failed to reproduce the essential radial secondary flow features as the vorticity increases. In the presence of milder vorticity at the 30.0° position, much better agreement was achieved.

At the duct outlet position, shown in figure 14, the agreement between the inviscid computation and the experimental data is good at $r^* = 0.1$. At $r^* = 0.3$ to $r^* = 0.9$, the agreement deteriorates much more than at the 77.5° position. The large discrepancies can be attributed to viscous effects which were not included in the inviscid code and which became predominant over curvature effects in the straight portion of the duct. Results from the viscous computation were not available at the duct outlet position since it was terminated at the 77.5° position in reference 2.

Overall Comparison

The comparison of the inviscid computation with the viscous computation for a turning duct geometry was undertaken to assess the capability of the inviscid code relative to the viscous code to predict the secondary flows in a geometry for which benchmark data existed. The inviscid computation required approximately an order of magnitude more CPU execution time than the viscous computation (exclusive of the potential solution) for a solution that, because of the inherent inviscid approximation, did not predict the secondary flows quite as well as the viscous solution. This is to be expected, since the inviscid code is an iterative solver of the Euler equations while the viscous code is a single pass solver of correction equations to an a priori potential solution. Other factors that should be considered in the overall comparison of the two codes include the amount of input data preprocessing required and the generality of the input geometry requirements. The viscous code requires a three-dimensional potential solution to obtain streamline coordinates and an initial pressure field and the version in reference 2 is currently limited to ducts of rectangular cross section. The inviscid code utilizes an input generator (ref. 6) that is an order of magnitude faster than the potential solver used for the viscous code. The input generator produces the geometrical coordinates from a minimum of geometry and flow variable information by using cubic spline fits for interpolation and extrapolation. The inviscid code can be used for stationary or rotating axial-flow, radial-flow, or mixed-flow turbomachine geometries, although small cusps may be required at the blade leading and trailing edges to minimize grid slope discontinuities.

SUMMARY OF RESULTS

The primary and secondary flows computed by the viscous Kreskovsky-Briley-McDonald code and the inviscid Denton code were compared with benchmark

experimental data for a turning duct. The viscous code is a fully parabolized space-marching Navier-Stokes solver while the inviscid code is a time-marching Euler solver. The experimental data were collected by Taylor, Whitelaw, and Yianneskis with a laser doppler velocimeter system in a 90° turning duct of square cross-section. The agreement between the viscous and inviscid computations was generally very good for the streamwise primary velocity, except at the walls, where slip conditions were specified for the inviscid code. Both computations failed to predict the distorted primary velocity profile shown by the experimental data near the suction surface at the 60.0° and 77.5° positions. The inviscid computation overpredicted the radial secondary velocity at the endwalls due to the imposed slip condition. Both computations failed to predict the strong reversals in the radial secondary velocity profile shown by the experimental data near the suction surface at the 60.0° and 77.5° positions. The inviscid compuation failed to match the experimental data at the duct outlet position due to the predominance of viscous effects over curvature effects in the straight portion of the duct. The comparison of the computations with the benchmark data has shown that both the viscous code and the inviscid code can provide useful information about secondary flow phenomena if the inherent limitations of each code relative to an elliptic Navier-Stokes code are recognized.

REFERENCES

1. Hah, C., "A Navier-Stokes Analysis of Three-Dimensional Turbulent Flows Inside Turbine Blade Rows at Design and Off-Design Conditions," ASME 83-GT-40, 1983.

2. Kreskovsky, J. P., Briley, W. R., and McDonald, H., "Prediction of Laminar and Turbulent Primary and Secondary Flows in Strongly Curved Ducts," NASA CR-3388, 1981.

3. Denton, J. D., "An Improved Time-Marching Method for Turbomachinery Flow Calculation," ASME 82-GT-239, 1982.

4. Taylor, A. M. K. P., Whitelaw, J. H., and Yianneskis, M., "Measurements of Laminar and Turbulent Flow in a Curved Duct With Thin Inlet Boundary Layers," NASA CR-3367, 1981.

5. McNally, W. D., and Sockol, P. M., "Computational Methods for Internal Flows With Emphasis on Turbomachinery," NASA TM-82764, 1982.

6. Glassman, A. J., and Wood, J. R., "Input Generator for Denton Three-Dimensional Turbomachine-Blade-Row Analysis Code," NASA TM-83324, 1983.

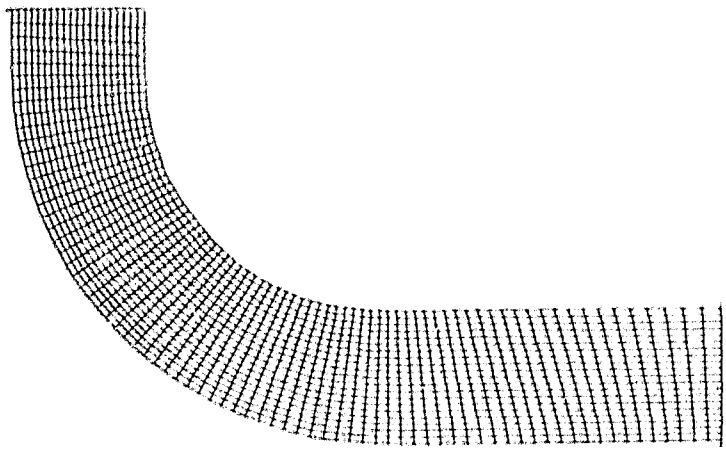

Figure 1. - Inviscid computational grid.

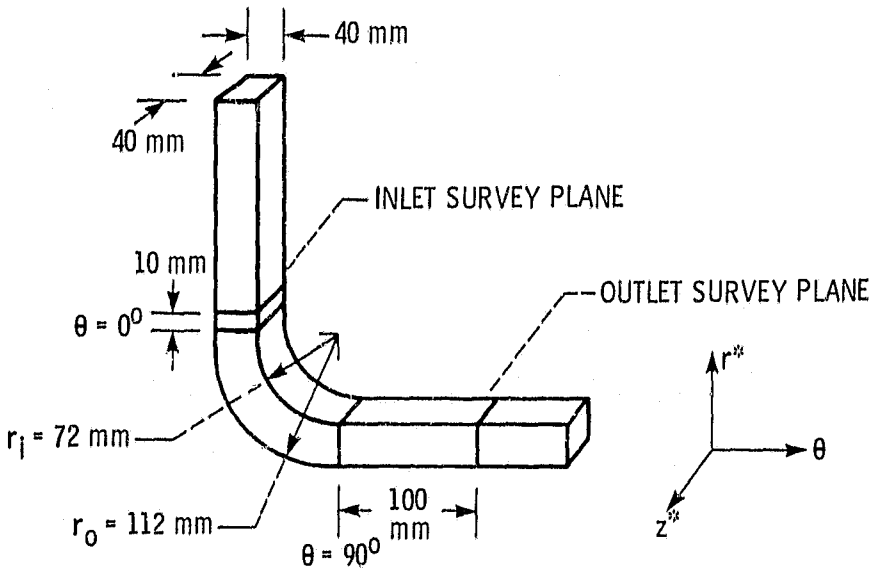

Figure 2. - Duct geometry.

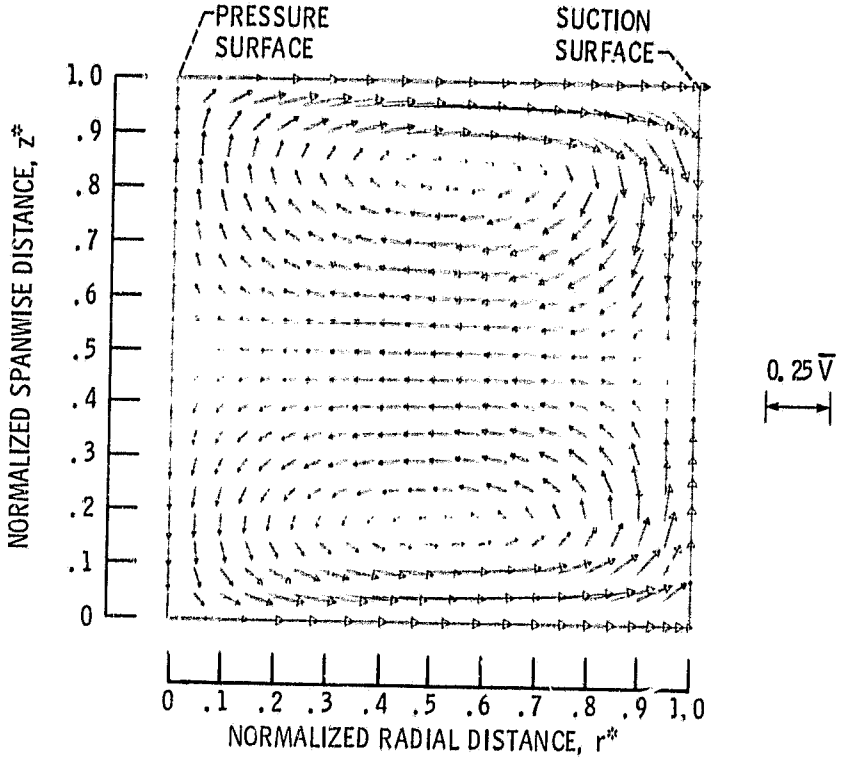

Figure 3. - Inviscid computation secondary flow field at 30.0° position.

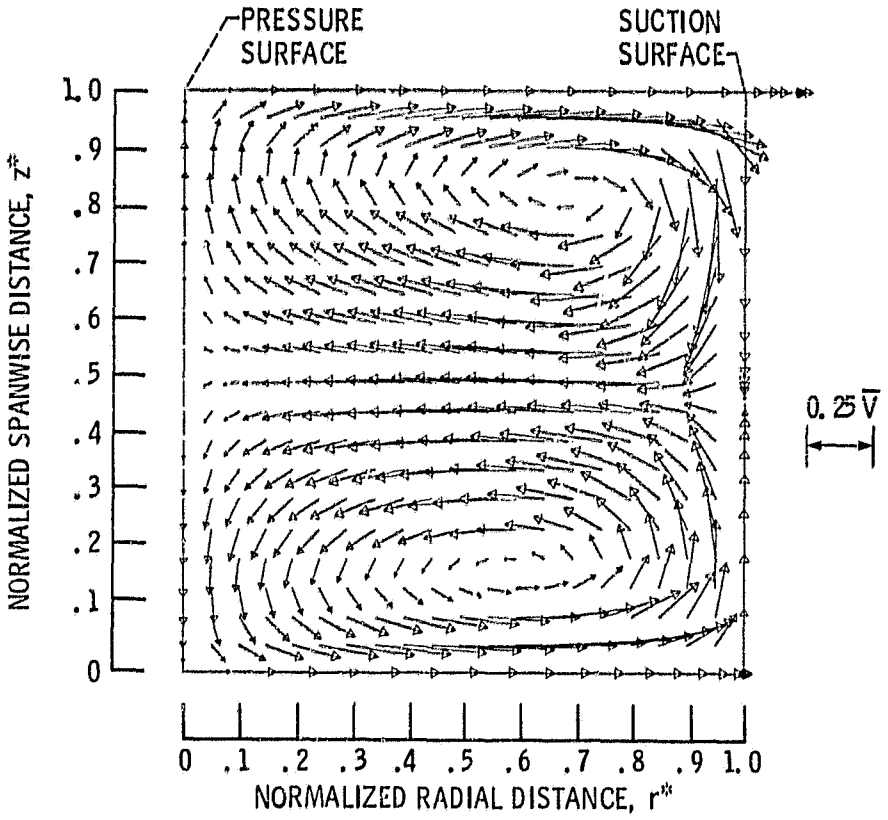

Figure 4. - Inviscid computation secondary flow field at 60.0° position.

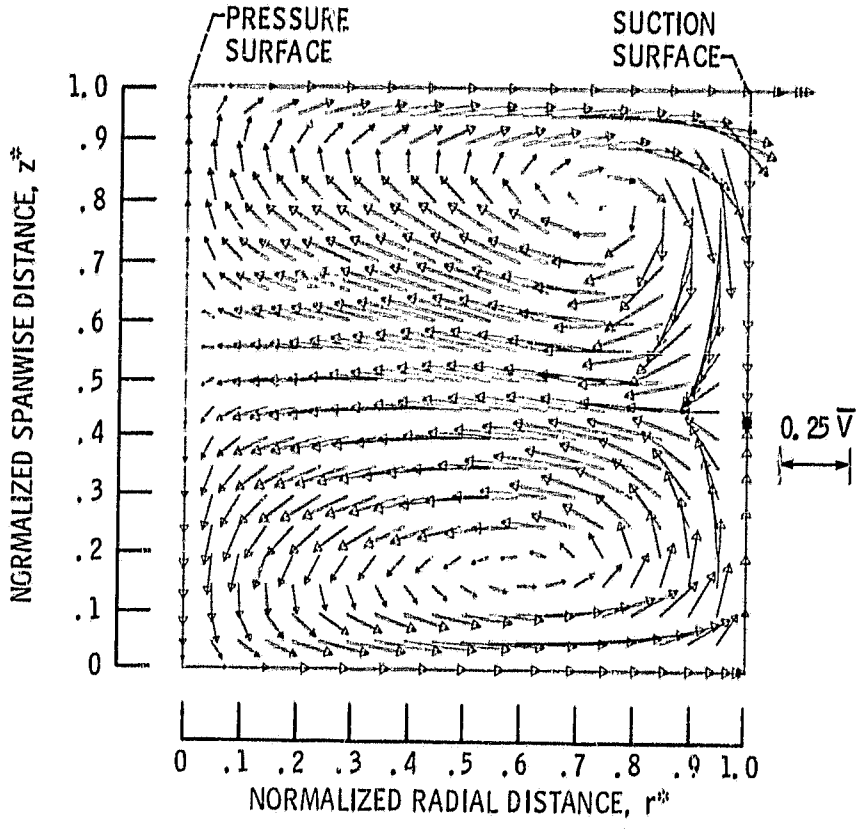

Figure 5. - Inviscid computation secondary flow field at 77.5° position.

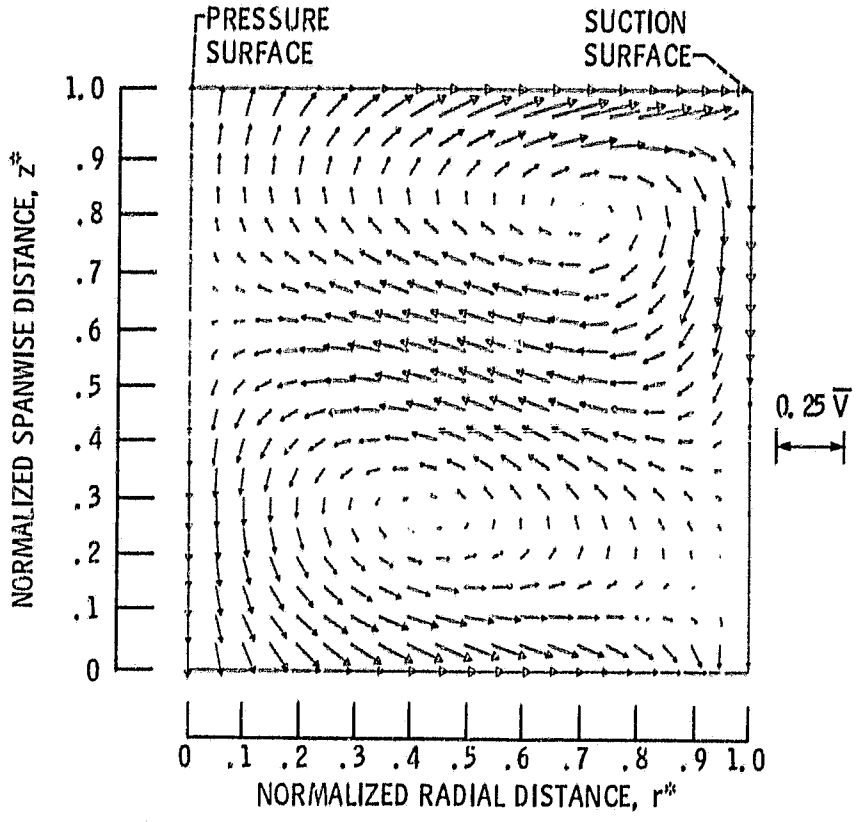

Figure 6. - Inviscid computation secondary flow field at duct outlet position.

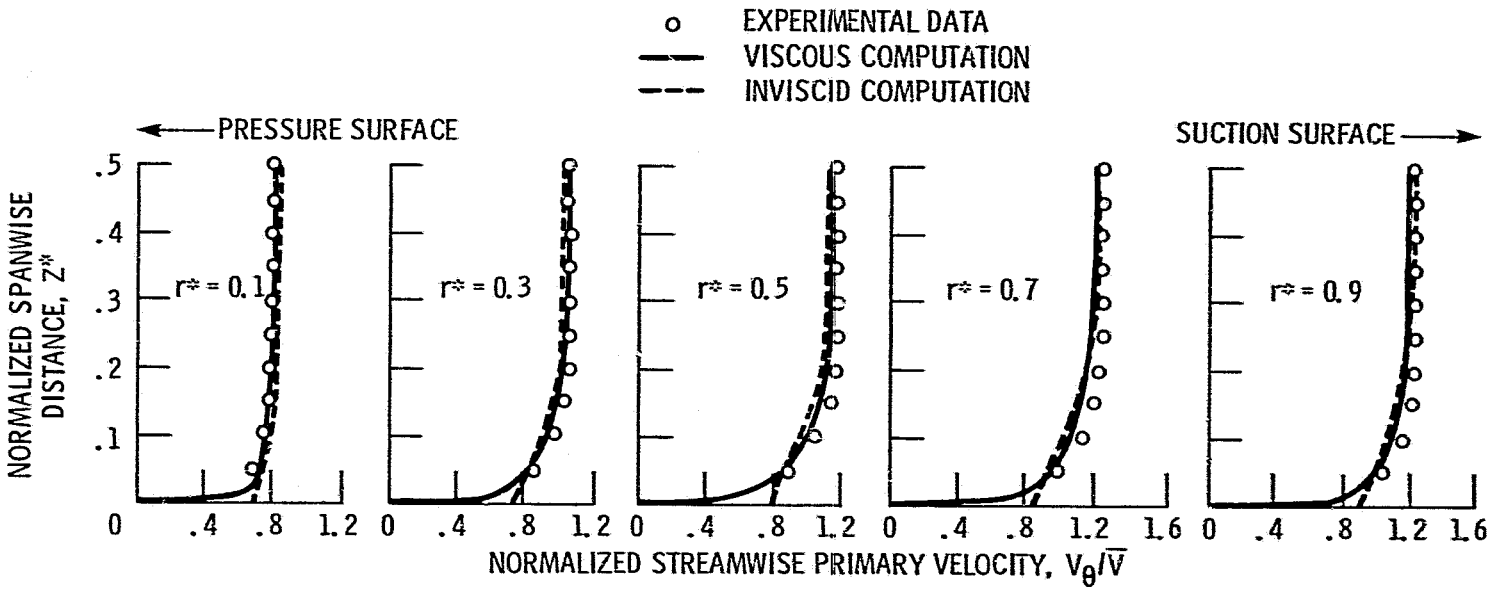

Figure 7. - Streamwise primary velocity profiles at 30.0° position.

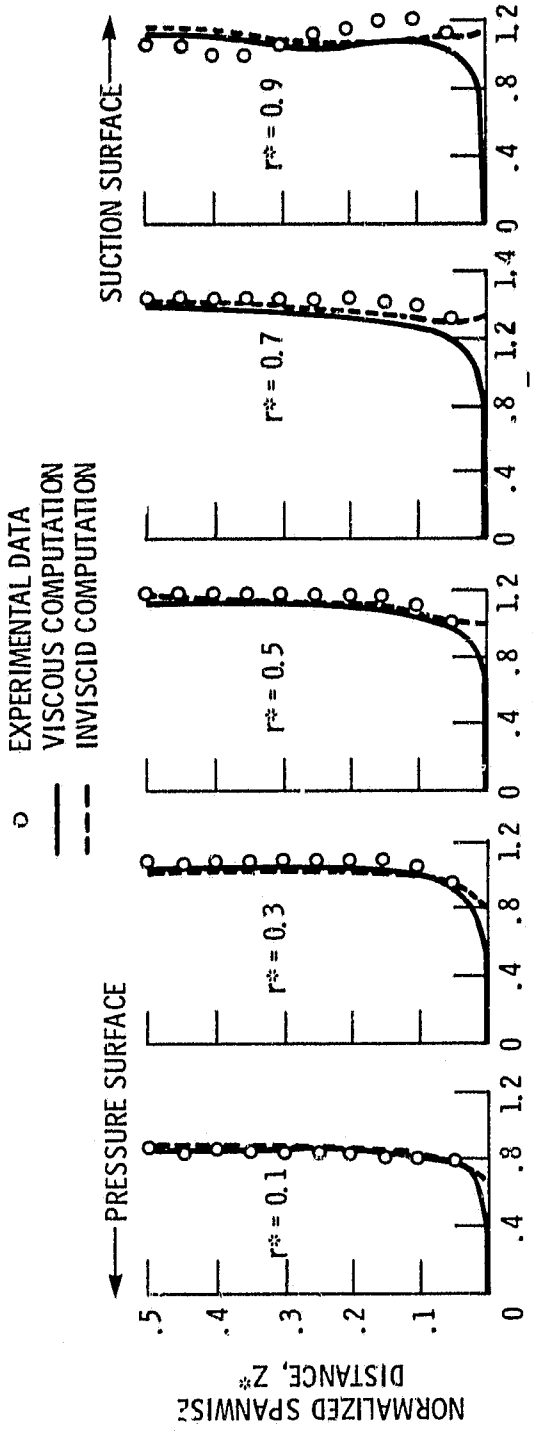

Figure 8. - Streamwise primary velocity profiles at 60.0° position.

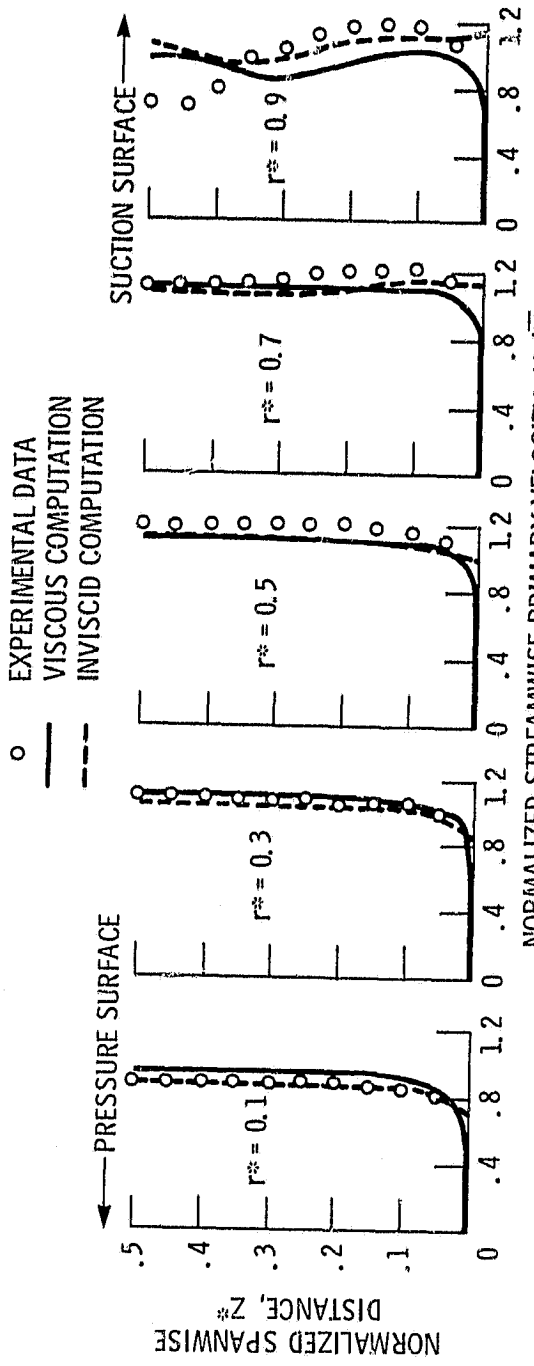

Figure 9. - Streamwise primary velocity profiles at 77.5° position.

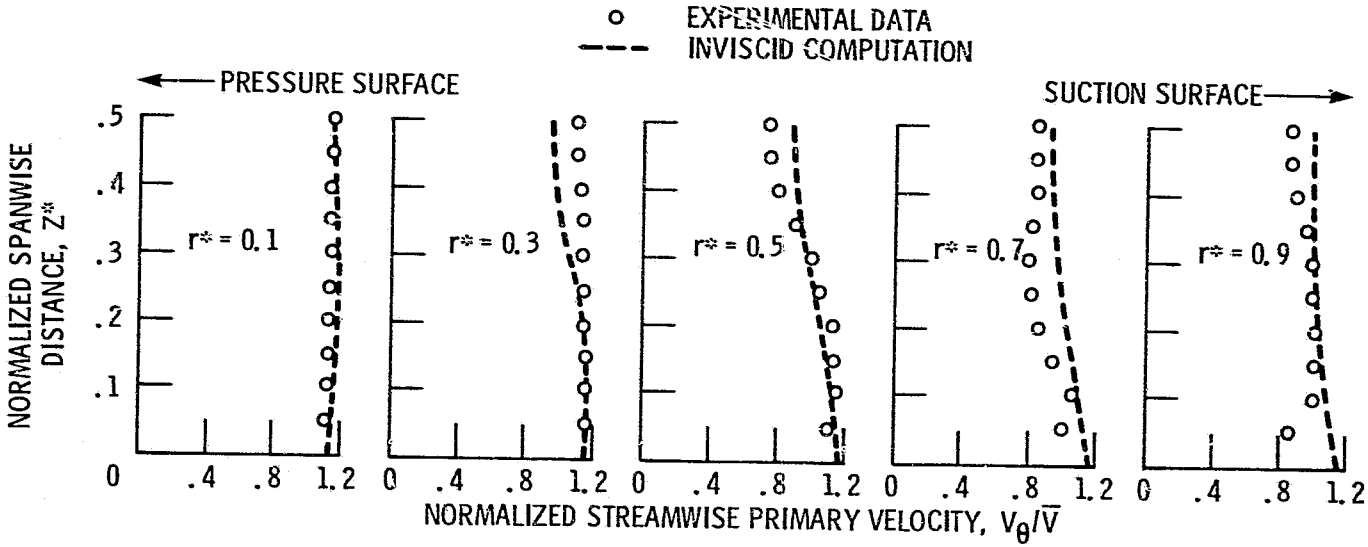

Figure 10. – Streamwise primary velocity profiles at duct outlet position.

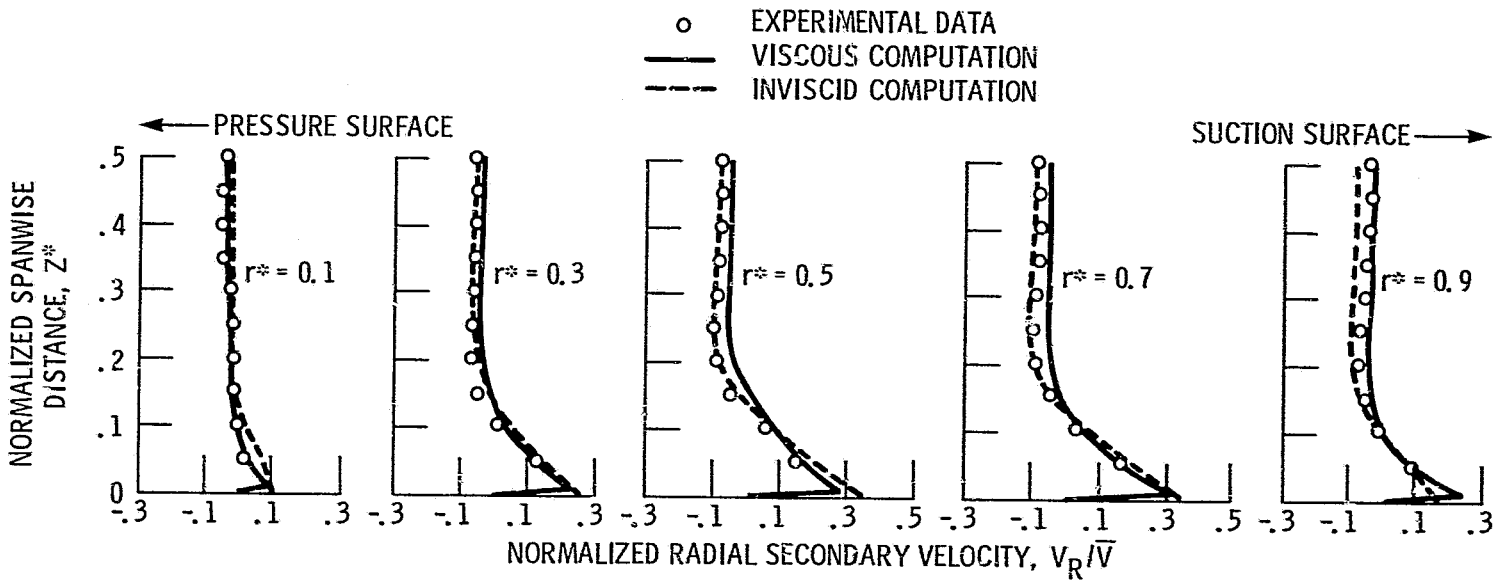

Figure 11. - Radial secondary velocity profiles at 30.0° position.

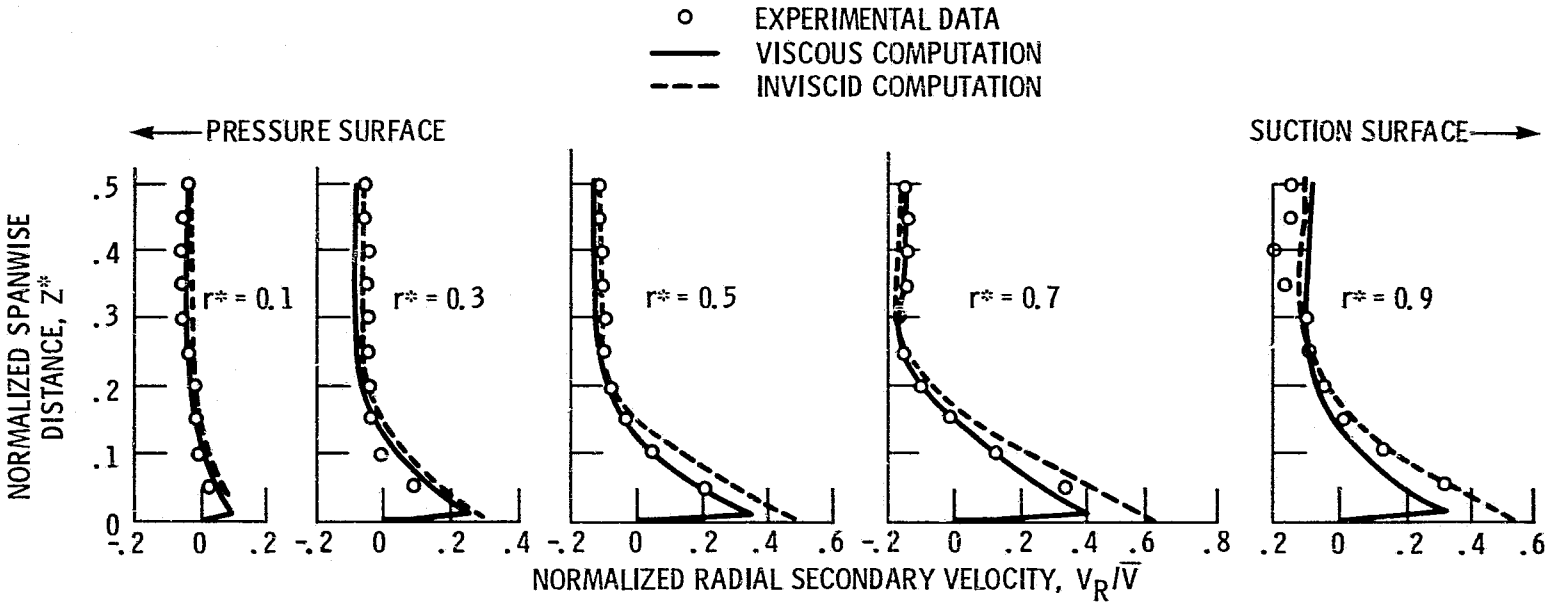

Figure 12. - Radial secondary velocity profiles at 60.0° position.

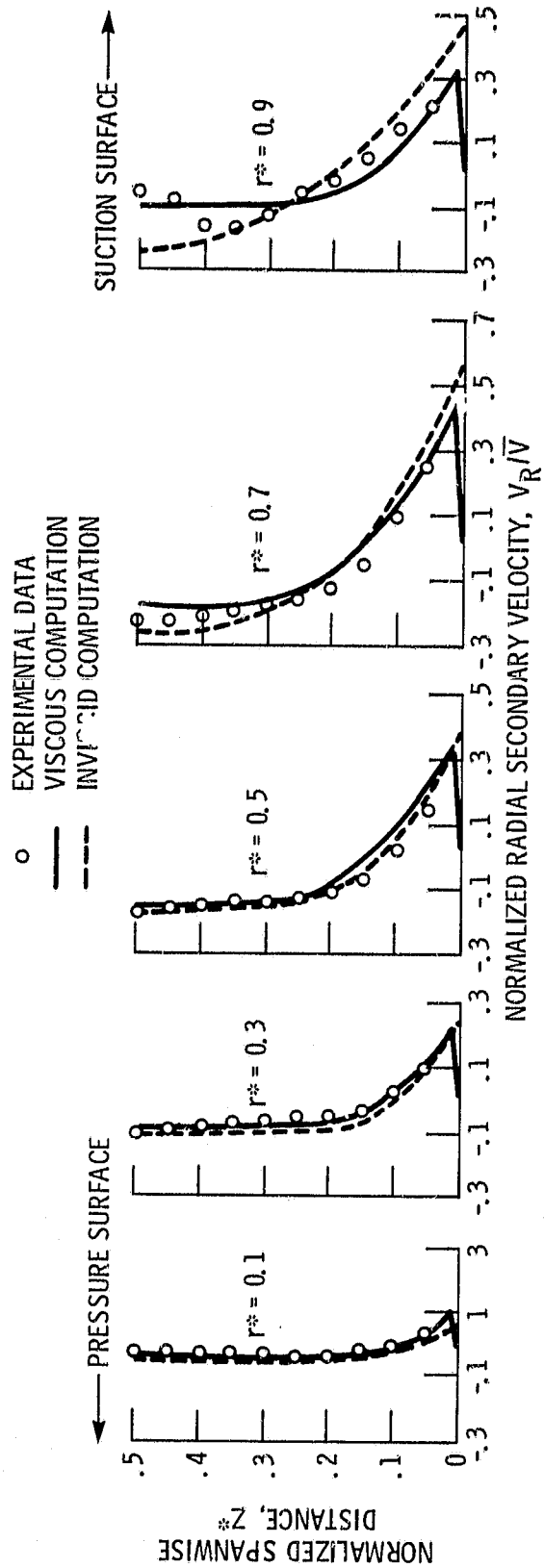

Figure 13. - Radial secondary velocity profiles at 77.5° position.

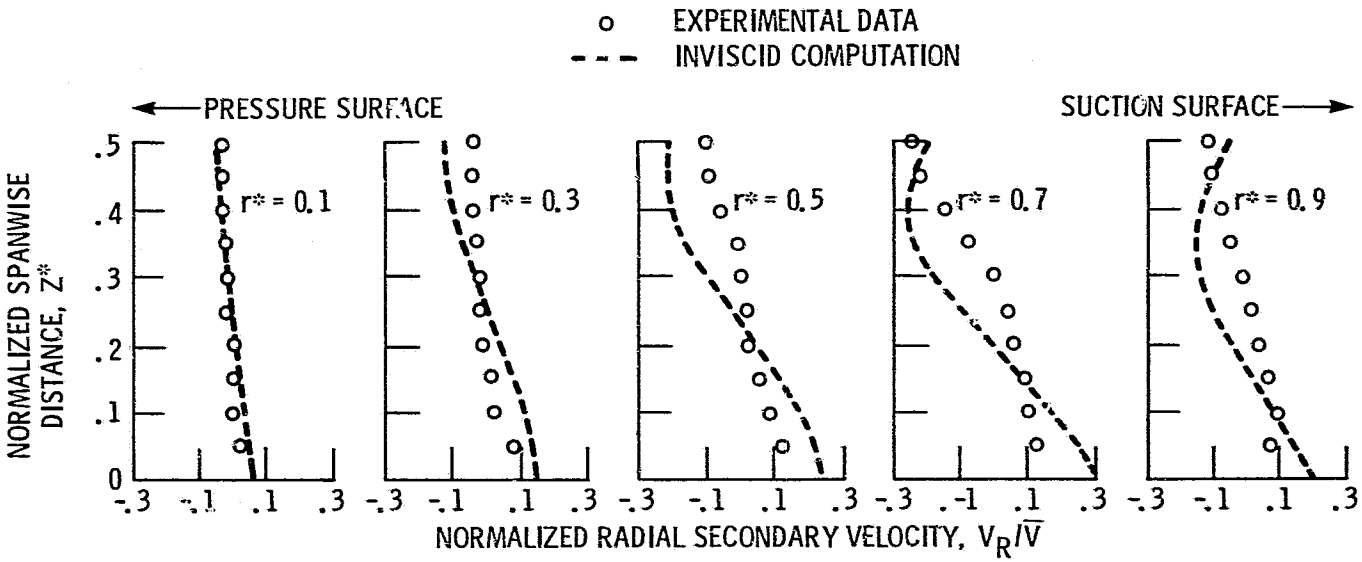

Figure 14. - Radial secondary velocity profiles at duct outlet position.